## ARTICLE

OPEN

Check for updates

# Anticounterfeiting tags based on randomly oriented MoS$_x$ clusters enabled by capillary and Marangoni flow

Changgyun Moon[1,7], Pavan Pujar[2,7], Srinivas Gandla[1,7], Byungjun So[3,7], Sunjong Lee[4], Dongmin Kim[4,5], Kon-Woo Kwon [6,8✉] & Sunkook Kim [1,8✉]

Recent advances in anticounterfeiting technology highlight the importance of functional materials with innovative processing methods for achieving robust anticounterfeiting tags. Here, we report a fabrication approach that enables the formation of randomly oriented MoS$_x$ or MoO$_x$ clusters of unpredictable shapes for use as anticounterfeiting tags. We exploit the combined effects of capillary and Marangoni flows to drive solute in a pre-deposited wet film that produces random clusters, creating tags. The reading of these tags is achieved using high-speed confocal laser microscopy, which allows for the extraction of complex topographies in seconds. The digitization of the tags involves converting height profiles into grayscale images, followed by the application of mathematical tools and the von Neumann debiasing technique. The extracted keys are subjected to the NIST statistical test, which consists of six tests to confirm the randomness of the generated keys. The recent advancements in anticounterfeiting technology highlight the importance of functional materials with innovative processing methods to achieve robust anticounterfeiting tags.

[1] Multifunctional Nano Bio Electronics Lab, Department of Advanced Materials Science and Engineering, Sungkyunkwan University, Suwon-Si, Gyeonggi-do, Republic of Korea. [2] Department of Ceramic Engineering, Indian Institute of Technology (IIT-BHU), Varanasi, Uttar Pradesh, India. [3] Wafer Bonding Team, SK Hynix Company, Icheon, Republic of Korea. [4] Korea Institute of Industrial Technology (KITECH), Cheonan, Republic of Korea. [5] Yonsei University, Seoul, South Korea. [6] Department of Computer Engineering, Hongik University, Seoul, Republic of Korea. [7] These authors contributed equally: Changgyun Moon, Pavan Pujar, Srinivas Gandla, Byungjun So. [8] These authors jointly supervised this work: Kon-Woo Kwon, Sunkook Kim. ✉email: konwoo@hongik.ac.kr; seonkuk@skku.edu

The movement of liquids through narrow regions is mainly influenced by surface-driven flows, such as capillary flow. Additionally, the localized gradient in interfacial tension causes liquid particles to drift, leading to uphill flow along the surface or interfacial tension[1]. These flows have great implications in developing modern technologies such as printed electronics, where the nanoparticle-containing colloidal liquids are allowed to evaporate on a substrate, giving rise to stains of nanoparticles[2,3]. On thermal-assisted consolidation of these particles lead to the formation of a continuous network allowing the percolation of charge carriers. Other prominent applications involve sensors, skin electronics, and robotics[4–7].

On the other hand, the proliferation of counterfeit products poses a significant problem for any nation, in terms of its impact on health, the economy, and high-tech security[8,9]. An effective solution to this problem is the use of anti-counterfeiting tags attached to products. The anti-counterfeiting tag is a physical device that is unclonable, unpredictable, and difficult to reproduce, even for the manufacturer who initially produced it. Recently, there has been an increasing trend in anticounterfeiting tags based on chemical methods[10]. These chemical methods involve solution chemistry with large parameters that offer a large encoding data capacity and the necessary randomness for efficient anticounterfeiting tags[11–17].

Here, we present the essence of Capillary and Marangoni flow-driven metal-oxygen complexes in establishing a network like metal oxide clusters distributed randomly. The clusters are irregular or unpredictable in shape with a few micrometer-size features. The selective area ($50 \times 50$ μm$^2$) of a group of clusters serves as a tag for anti-counterfeiting purposes. The random morphology of the film is mainly governed by the interplay between capillary and Marangoni flows of liquid precursors containing two distinct solvents with large gradients in surface tension. The gradient establishes instability leading to surface-active flows. The liquid particles carry solutes, in other words, the solutes act as flow markers. On freezing, the solute particle stuck to the substrate in a pattern form dictated by the liquid particles. The obtained clustered pattern of solute undergoes transformation depending on the thermal budget. In the present investigation, this randomly clustered morphology is further investigated for its applicability as anticounterfeiting tags. The topography of randomly distributed metal-based clusters, converted to digitized keys, showed promising results with high entropy, bit uniformity, and reproducibility, confirmed through mathematical tools and statistical NIST tests. This study enables new opportunities for advanced functional materials producing advanced tags.

## Results and discussion

### Process flow: Random orientation of MoO$_x$/MoS$_x$ clusters.

The process adopted in the present study to randomly distribute the clusters of MoO$_x$/MoS$_x$ is described in Fig. 1. The workflow primarily involves fabricating, reading, and digitally generating tags. The steps for achieving morphology evolution and sulphurization are illustrated schematically in Fig. 1a–f. Random morphology can be obtained through two steps: (1) spin-coating of precursor and (2) thermal baking. The topography, obtained using 3D confocal laser microscopy to acquire a height profile, is shown in Fig. 1g. The digitization of 2D confocal images is carried out using various mathematical tools and algorithms, as depicted consecutively in Fig. 1h, i. A detailed discussion of this process is provided in the section on digitized key generation. Finally, the digitized keys are stored over the Internet for on-demand verification of tags at the retailer/customer end, as shown in Fig. 1j. A digitized form of a key of a tag is efficient for transferring and accessing over the cloud compared to a raw image file of a tag because a raw image file needs a huge data file to store and access.

### Precursor analysis and morphology evolution.

The morphology of solution-cast thin films is predominantly guided by the movement of solute particles (or molecules) in the pre-deposited wet film. The 'wet film' contains a large fraction of solvent, which on evaporation results in the stains of retained-solute. If the solute is of solid phase then the movement of it in the solution is guided by the flow of solvent within the confined geometry of the film[18,19]. This flow is affected by various factors, one major factor is the evaporative loss of the solvent, mainly at the three-phase points in the geometry. To understand the same, first, the present molybdenum-containing precursor is drop-casted on a SiO$_2$ substrate, and the resulting morphology with room temperature evaporation is investigated (Fig. 2a). The morphology is greatly affected by the geometry of the sessile drop, the geometry of the drop is guided by the volume of the liquid dispensed, the radius of the drop ($r$), surface tension (σ), and the contact angle (θ). Both σ and θ are measured using same characterization system, firstly, the value of θ is recorded by dispensing a fixed volume of precursor on to SiO$_2$ and second, the magnitude of σ is determined using pendant drop method, where the precursor drop is allowed to suspend at the syringe outlet against gravity and the force required is characterized from the inbuilt system software. The drops with small θ are preferred for the uniform spreading of precursor on SiO$_2$, thus, reducing σ is first considered. To accomplish the same, a low-σ organic solvent, 2-methoxyethanol (2-ME) is mixed with the precursor with different volume fractions. Both 2-ME (cosolvent) and DI water are miscible thus, proper mixing is ensured at all volume fractions of 2-ME. It is found that with an increase in the fraction of cosolvent 2-ME, the system was found to attain low-σ, thereby small-θ (Fig. 2b, c). The reduced-θ attains a saturation with 10 % (volume basis) of 2-ME concentration in the precursor. The nonlinear curve fitting reveals that a minimum of 10 vol% is required to attain the θ, as minimum as 12–13°. Further addition of 2-ME may not significantly affect the θ, but it greatly affects the σ. The reduction in the σ is useful to tune the Marangoni flow in the droplet[19].

It was largely investigated in reported studies that the presence of intense Marangoni flows is known to reverse the ring stain deposits[19]; a similar observation has also been made in the present study. The Marangoni flow is a surface tension-driven movement of fluid particles. The difference in the surface tension results in the flow of fluid from low-surface tension regime to high surface tension regime. The localized gradient in surface tension owing to the presence of varied concentration of 2-ME (a low surface tension solvent) added with annealing temperature intensifies the Marangoni flow. Further, the capillary flow is the volume resulting from the loss of precursor mass at the pinned edge of the droplet. The movement of fluid particles from the center of the drop top the edge carries the passive solid phase. These solid particles stuck at the edge of the drop due to evaporative loss of the precursor. Both Marangoni and capillary flows result in different morphologies (i.e., edge deposit due to capillary flow and center deposit due to Marangoni flow) as presented in Fig. 1d, e. The ring-stain morphology is observed on the room temperature drying of the pure DI-based precursor. On the other hand, the extensive Marangoni flows, reverse this effect and thus result in the center deposit (Fig. 2d, e). These two extremities need to be avoided to achieve the required random morphology. To accomplish the same, a series of trials with varying volume fractions of 2-ME is drop-casted and the resulting morphology has been investigated. For precursors with 50 and 40 vol% 2-ME, the resulting morphologies are recorded (Fig. 2g), in both cases, the random distribution of Mo-salt on the substrate is the result of mixed capillary and Marangoni flows.

### Probabilistic mechanism of random morphology.

2-ME is a volatile organic solvent when mixed with DI water, 2-ME evaporates
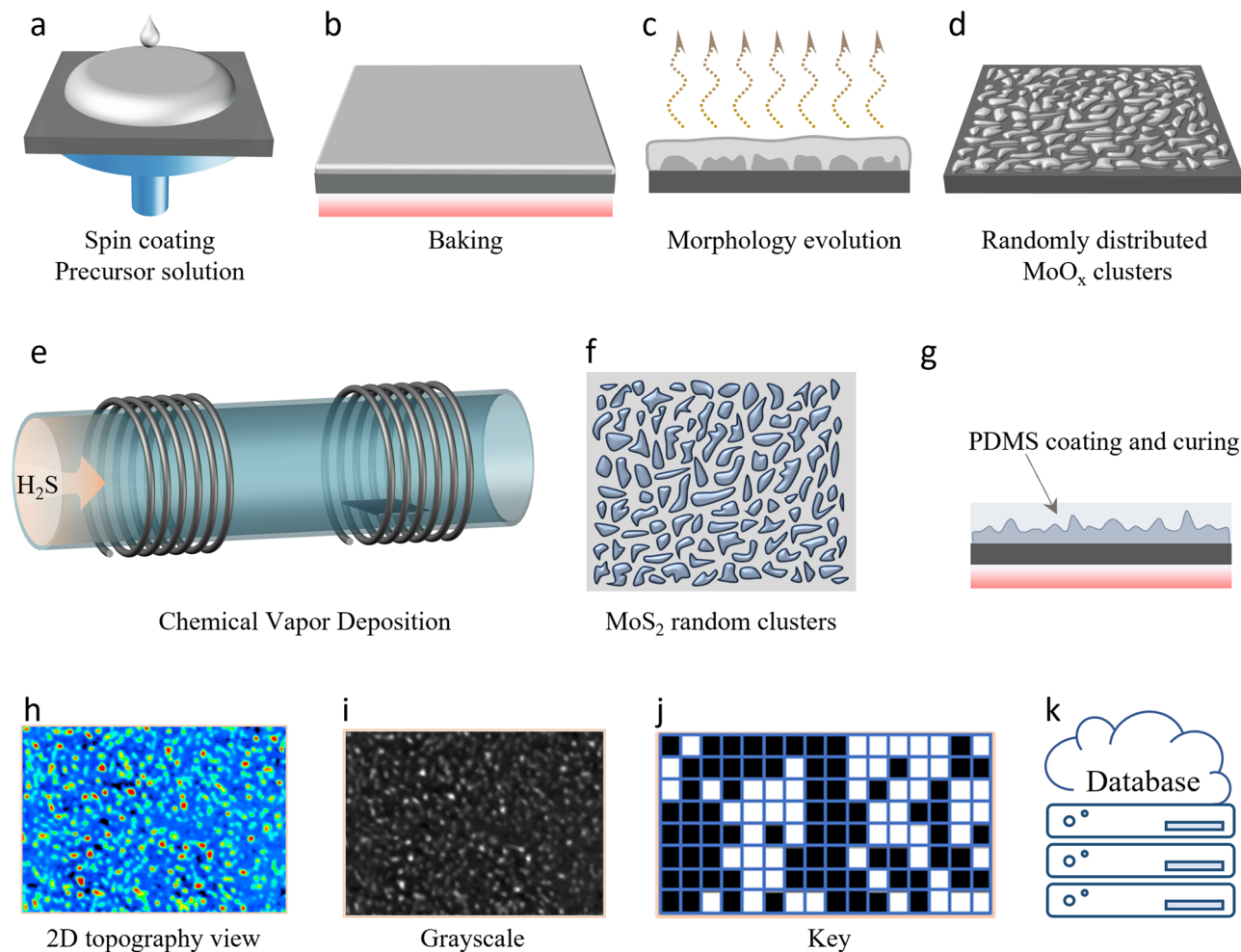
**Fig. 1 Overview of MoS_x random clusters as tags for anticounterfeiting purposes.** Morphology evolution of $MoO_x$ clusters: schematic showing **a** metal-oxide precursor spin-coating, **b** baking process, **c** morphology evolution governed by Capillary and Marangoni effects, **d** randomly distributed clusters. **e** Sulfurization using $H_2S$ gas by a CVD process. **f** Schematic representation of randomly distributed $MoS_x$ clusters. **g** PDMS spincoating followed by curing on a hotplate. **h** 2D height profile view of $MoS_x$ random clusters obtained via 3D laser confocal microscopy. **i** Grayscale image and its **j** key generation process based on **i**. **k** Storage of digital keys over the Internet for on-demand verification of tags.

more quickly compared to DI water. The room temperature evaporation is driven by the vapor pressure gradient. 2-ME is thermodynamically more unstable and thus more volatile in room temperature processing. The large evaporative flux at the three-phase point creates a region of deficient 2-ME (Fig. 1f), to replenish the loss of mass at the pinned boundary of the drop, the liquid from the center of the drop flows towards the edges (i.e., capillary flow). However, DI water with dissolved Mo-salt at the boundary becomes nearly free of 2-ME, thus, a relatively high σ of DI allows it to form spherical droplets (Fig. 2f) which are free to move in the liquid regime (within the drop). During this, these droplets undergo coalescence and become large in volume. On evaporation, they leave behind Mo-salt at random locations in the dried stain.

The creation and movement of these DI water droplets are guided by the volume fraction of 2-ME. Given these, a precursor with a large fraction (i.e., 50 vol%) of 2-ME is considered for further investigation. The thermal decomposition of Mo-tetrahydrate to form the oxide of molybdenum ($MoO_x$) is further investigated using thermogravimetric analysis coupled with differential thermal analysis of the precursor (Supplementary Fig. 1). These results convey that the formation of $MoO_x$ requires a minimum temperature of 350 °C. Although extending the bulk precursor thermal analysis to its thin film counterpart is debatable[20,21], however, it provides a rough estimation of annealing temperature.

Thus, on thermal annealing, the randomly distributed crystals of Mo-tetrahydrate decompose to form $MoO_x$. Subsequently, $MoS_x$ was formed through the sulfurization of the $MoO_x$ thin film using vacuum CVD processing at 1000 °C. The detailed sulfurization process is provided in the supporting information, following Supplementary Fig. 2. The formation of $MoS_x$ was confirmed through Raman spectroscopy. The Raman mapping images ($E_{2g}$ and $A_{1g}$) obtained from a section of the $MoS_x$ tag are shown in Supplementary Fig. 3. These images, displaying the $E_{2g}$ (in-plane vibration) and $A_{1g}$ (out-of-plane vibration) peaks, exhibited a distribution pattern similar to the random clusters shown in Fig. 3b. These two peaks were observed at approximately 383 $cm^{-1}$ and 408 $cm^{-1}$, confirming the formation of $MoS_x$. The randomly distributed $MoS_x$ clusters were organized into $4 \times 5$ blocks, with each block serving as a tag.

It should be noted that $MoO_x$ possesses a bandgap of approximately 3.2 eV, rendering it transparent to a 661 nm wavelength (which was utilized for obtaining the 3D profile of the cluster morphology). Consequently, measuring the profile with this wavelength source is not feasible, and alternative wavelength sources must be employed. Furthermore, the inclusion of the synthesis of $MoS_x$ was presented to highlight its potential in enabling a multifunctional authentication mechanism. Recent developments in authentication protocols aim to expand the total
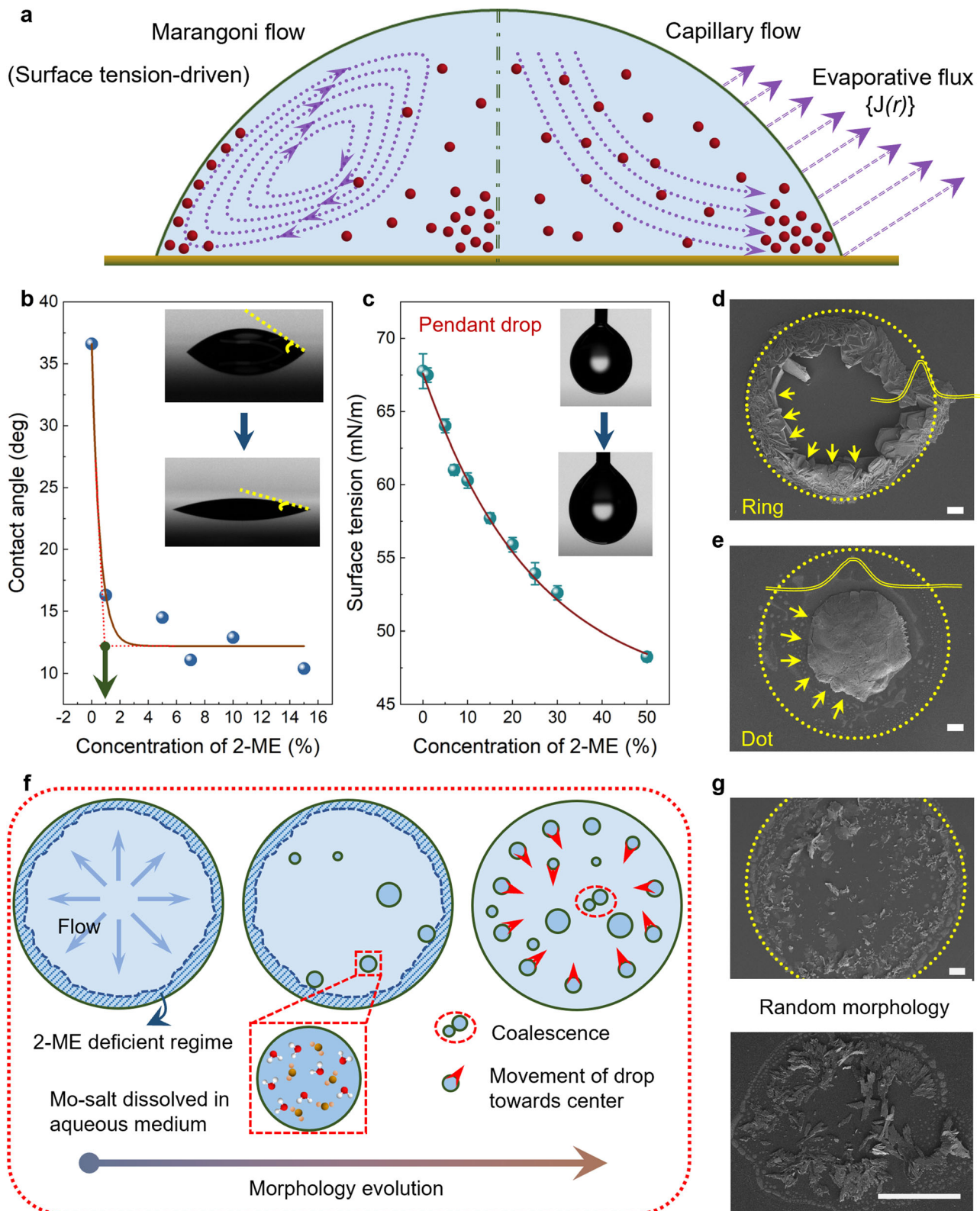
**Fig. 2 Morphology evolution. a** Schematic depicting the capillary and Marangoni flow in a sessile droplet on a substrate, where $J$ and $r$ represent the evaporative flux and the radius of the sessile drop, respectively; the arrow marks show the evaporation of the drop that is high at the pinned edge (i.e., three-phase point) of the drop. Variation of **b** contact angle and **c** surface tension with the concentration of 2-ME in the precursor. The scanning electron micrographs of **d** ring **e** center (dot) deposits (scale: 100 μm). The qualitative height profiles depict the region of deposition, in the case of **d** it is the edge and in the case of **e**, the deposit is at the center. **f** Steps in morphology evolution and **g**, **h** random morphology of Mo-precursor.
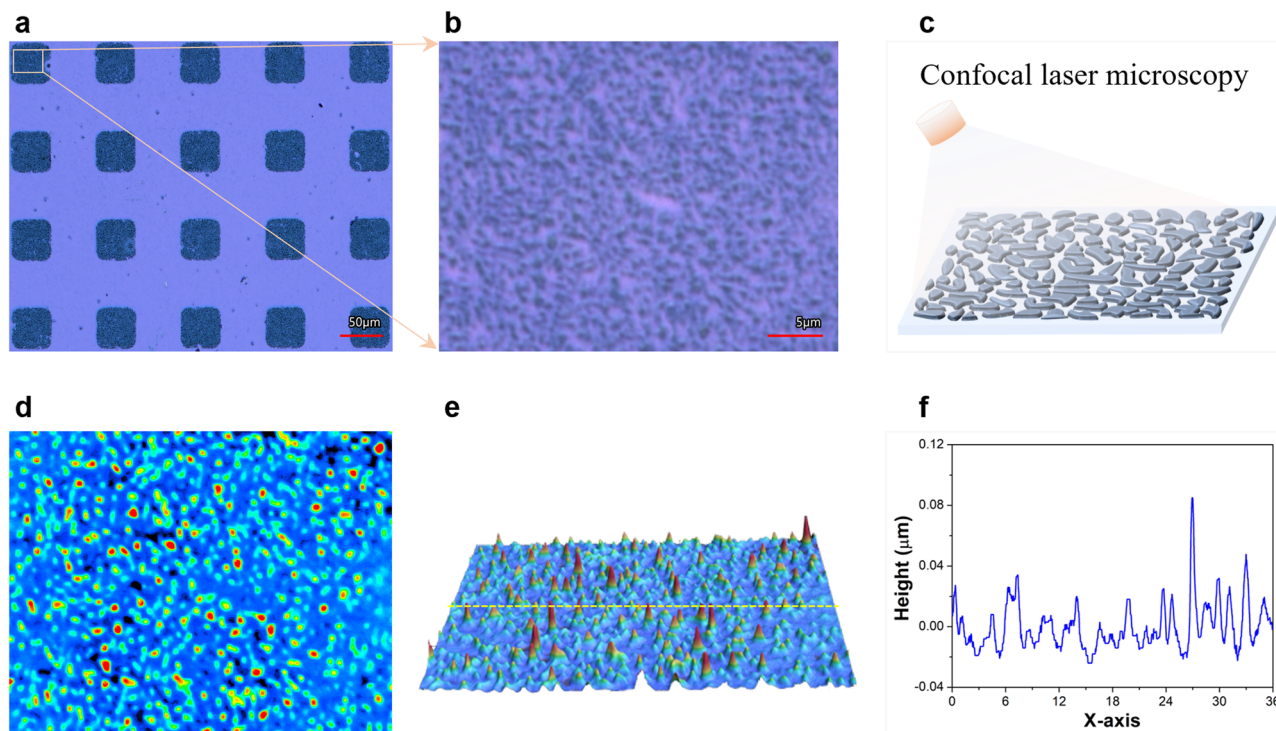
**Fig. 3 Random clusters 3D profile. a** Optical micrograph of the $MoS_x$ tags (4 × 5 pixels) with **b** inset showing the tag's enlarged view of random clusters. **c** Schematic illustrating the confocal laser scanning of a randomly distributed $MoS_x$ clusters topography. The **d** 2D and **e** 3D topography view profiles of tag 1. (f) Randomly selected 1D line height profile along the middle of the $MoS_x$ tag.

size of the key space[22]. $MoS_2$, in contrast to $MoO_x$, offers two additional features: electrical and optical dichroism properties. In conclusion, the synthesis of $MoS_x$ was undertaken to demonstrate its effectiveness as a potential candidate for anti-counterfeiting tags. While anticounterfeiting tags based on $MoS_2$ physically unclonable devices have been reported in previous studies[23–26], it is important to note that reading these devices often necessitates the use of expensive characterization tools. In contrast, our current approach provides an alternative method that employs a less complex and more affordable confocal laser microscopy tool. A comparison of our work with previous studies is presented in table form (Supplementary Table 1).

**$MoS_x$ clusters 3D profile**. The topography of $MoS_x$ clusters along the x, y, and z axes was scanned using rapid 3D confocal laser microscopy in a layer-by-layer fashion. The raw optical micrographs and the 3D confocal laser scanning processes involved in acquiring 2D and 3D profiles are shown in Fig. 3. The optical micrographs of the patterned $MoS_x$ tags, with an inset showing an enlarged view of one tag, are displayed in Fig. 3a, b. It should be noted that the feature sizes of the $MoS_x$ clusters are approximately 1.25 μm (Supplementary Fig. 4), making it uncertain to obtain a good resolution of individual clusters through optical microscope imaging. Therefore, recapturing and confirming the same tag is crucial. Consequently, laser confocal imaging is employed to extract the essential characteristics (clusters) of the tag. Laser confocal imaging offers several advantages, including an ambient scanning environment, large-area scanning, a faster scanning process, and less training required due to its impeccable system. Importantly, as the laser light source operates in the visible region, it is also possible to scan tags with a protective transparent coating on top, effectively avoiding replication or duplication through molding techniques. Laser confocal imaging utilizes a single, parallel laser beam to focus on a specific point in the sample, which is then selectively reflected through a small

aperture onto a detector to filter out unwanted scattered light. By eliminating unwanted scattered light, high-resolution imaging is achieved. The laser scans successive x-y planes in a layered fashion along the z-direction to capture complex topography. An area of $36 \times 27$ μm$^2$ is selected for scanning the topography of the tag samples. Typically, a maximum area of around $450 \times 450$ μm$^2$ (20×) in the x-y plane can be accomplished with a minimum resolution down to 100 nm in less than 60 s. Figure 3c presents an oversimplified schematic of laser confocal microscopy during scanning. The extracted 2D and 3D views of the topography of the tag clusters are displayed in Fig. 3d, e and Supplementary Fig. 5, while Fig. 3f shows the 1D profile across the horizontal center.

**Digital key generation process**. The flowchart outlining the extraction process of digital keys from 2D topographical tag images is illustrated in Fig. 4. Twenty distinct $MoS_x$ responses are prepared, as explained in Fig. 3, serving as the basis for generating the digitized keys (Fig. 4a). The raw data from these responses undergo height profiling, followed by the conversion into a grayscale image utilizing our custom Python code (Fig. 4b). To enhance the quality of the image, the denoising process is conducted with Non-Local Means (NLM) algorithm[27]. Subsequently, the peak_local_max function from the scikit-image open-source library is employed to detect the local peaks in the image. The identified peaks in the image are then converted to binary digits, with '1' representing local peaks and '0' assigned to all other positions. To ensure reproducibility, the binarized image is resized to a consistent size of 28 pixels × 20 pixels using a binning process that combines the bits into predetermined dimensions (Fig. 4c). In our case, the occurrence of 0-valued pixels is consistently higher than that of 1-valued pixels, resulting in bias towards 0 values (Supplementary Fig. 6). To achieve a more balanced bit uniformity of approximately 0.5, the von Neumann debiasing technique is utilized, however, the extracted keys are
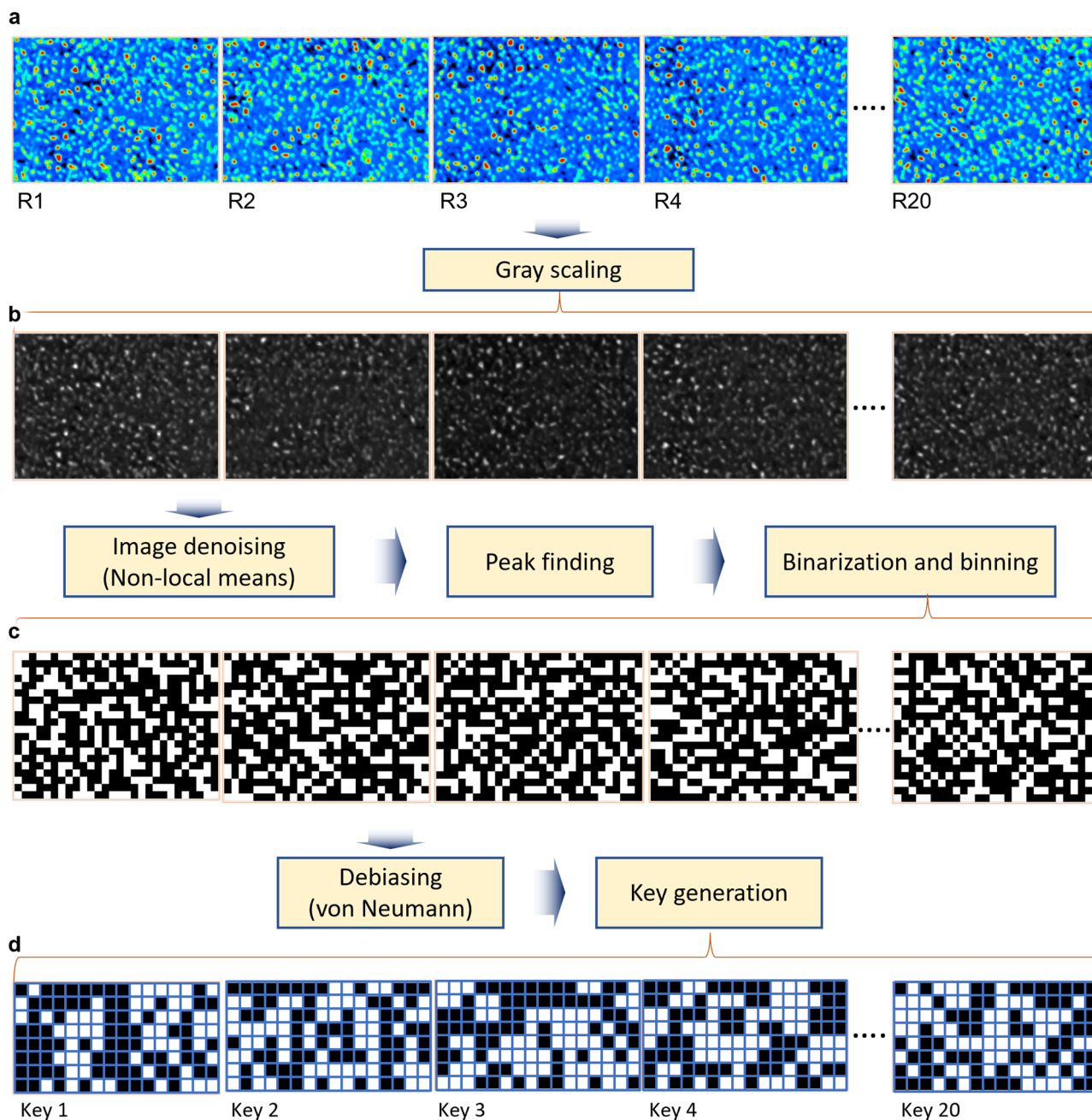
**Fig. 4 Flow-diagram showing digital keys generation from MoS$_x$ 2D topography images. a** MoS$_x$ tags 2D topography (height profile) images (responses) obtained from a confocal laser microscope. **b** Conversion to grayscale images followed by denoising by non-local means, peak finding, and **c** binarization and binning. **d** Key generation of 128 bits each (8 × 16) after applying Von-Neumann debiasing.

nonuniform (Supplementary Fig. 7)[28]. Therefore, the first 128 bits are selected as the digital key to ensure a consistent final key length (Fig. 4d).

**Characterization of tags**. To evaluate the performance of the tag system, essential characteristics such as entropy[29,30], bit uniformity, reproducibility (intra-device HD), uniqueness (inter-device HD), degree of freedom, and false negative, positive rates of each tag are investigated[31]. The entropy of the tag is defined[32]:

$$E = -\left[p\log_2 p + (1-p)\log_2(1-p)\right];  \quad (1)$$

where $p$ is the probability of obtaining "1", from 128 bits of a tag. The calculated entropy for 20 tags is graphetically shown in Fig. 5a, using Eq. (1). The average entropy of 20 keys showed

mean and standard deviation (SD) values of 0.9938 and 0.0088, which is close to an ideal value of entropy '1' which indicates that the distribution has the maximum possible uncertainty or randomness. The bit uniformity in each tag occupies the probability of 0- and 1-bit states in a digitized key and is defined:

$$Bit\ uniformity = \frac{1}{s}\sum_{l=1}^{s} K_l  \quad (2)$$

Where $K_l$ is the $l$th binary bit of the key and s is the size of the total key. The mean value of digitized keys out of 20 unique tags returns the nearly ideal value of 0.4992 (the ideal value of bit uniformity is 0.5) and SD of 0.0461 (Fig. 5b). The reproducibility of key generation can be appraised by calculating the hamming distance (HD) of intra-device when the same challenge is applied
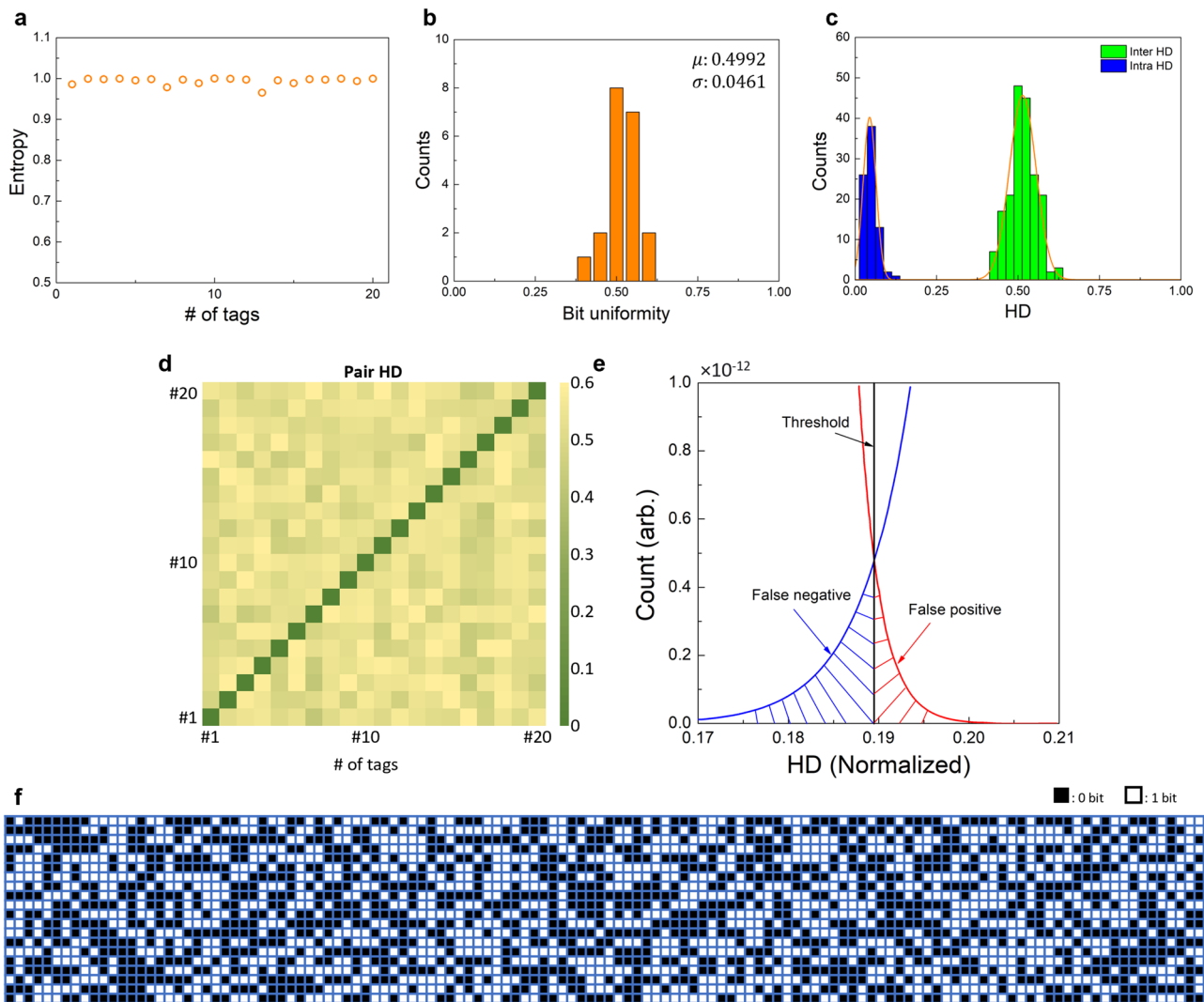
**Fig. 5 MoS$_x$ tags performance characterizations. a** Entropy and **b** bit uniformity of 20 tags. **c** Reproducibility (intra) and uniqueness (inter) among pairs of MoS$_x$ tags: intra case 20 pairs while inter case 380 pairs. **d** Heat map representation of intra-and inter-cases among the 20 tags: intra-cases along the diagonal while inter-cases off the diagonal (190 pairs on either side of the diagonal). **e** Extracted false positive, and negative rates. A cutoff threshold (HD = ~0.19) is determined based on the intra-and inter-HD distributions. This indicates a clear separation between the two intra and inter-distributions. **f** A combined binary bitstream of 20 different MoS$_x$ tags.

to the same tag at different times[16,33]. For this test, 4 repeated challenge-response pairs of each tag (4 pairwise comparisons) were used. The HD between pair of keys is calculated by comparing two bit streams $K_i$ and $K_j$ with a s-bit key being contrasted[16,33].

$$Hamming\ Distance(HD) = \frac{\#(K_i \neq K_j)}{s} \quad (3)$$

$$Reproducibility = \frac{1}{m}\sum_{t=1}^{s}\frac{HD(K_i, K_{i,t})}{s} \quad (4)$$

$$Uniqueness = \frac{2}{q(q-1)}\sum_{t=1}^{s}\frac{HD(K_i, K_{i,t})}{s} \quad (5)$$

where $K_{i,t}$ represents the s-bit keys of the i$^{th}$ tag at t$^{th}$ times among m different acquisition numbers from the source. The uniqueness of the key can be evaluated by calculating the HD of the inter-device, which shows the difference in the bitstreams among the two different keys. Suppose say, digitized keys from randomly chosen two tags are ideally uncorrelated, the HD of inter-device becomes 0.5. Particularly, when two keys are

compared, half of the key responses should be different from each other. The main difference between the reproducibility and uniqueness of the tag system is whether using other tags or using only a single tag for the comparison. Furthermore, the digitized key's encoding capacity from a single key was evaluated. The encoding capacity is defined as c$^s$, where C is the level of the bit and s is the size of the key. A MoS$_x$ tag has a 128-bit of key size and binary sequence (c = 2), showing a nominal encoding capacity of $2^{128}$. But, in real cases, the encoding capacity could be less than the nominal one because the result of the sequence is not independent completely. Therefore, the exact number of independent variables or degree of freedom is computed.

$$Degree\ of\ freedom = \frac{p(1-p)}{\sigma^2} \quad (6)$$

where $p$ is the value of mean probability and $\sigma$ is the value of SD[34]. From the distribution of inter-device HD, the key size of mutually independent bits is 138.41 ($\approx 0.5022 \times (1 -- 0.5022) \div (0.0425)^2$), still resulting in a high encoding capacity of $2^{138}(\approx 3.459 \times 10^{41})$. Not only the potential for storage data but also the randomness of solution-based MoS$_x$ tags supported by the high independence of

**Table 1 NIST statistical test results.**

| NIST statistical test | p-value | Proportion | Result |
|---|---|---|---|
| Frequency | **0.115387** | **1** | Pass |
| Block frequency | **0.115387** | **1** | Pass |
| Runs | **0.153763** | **0.95** | Pass |
| Longest run | **0.115387** | **0.95** | Pass |
| Serial | **0.062821** | **1** | Pass |
| | **0.085587** | **1** | Pass |
| Approximate entropy | **0.115387** | **0.95** | Pass |
| Cumulative sums (Forward) | **0.153763** | **1** | Pass |
| Cumulative sums (Reverse) | **0.085587** | **1** | Pass |

NIST statistical tests were conducted on 20 sequences (20 $MoS_x$ tags), each consisting of 128 bits (for a total of 2560 bits). The chi-squared ($\chi^2$) distribution was used to assess the goodness-of-fit by comparing the p-value distribution with an assumed distribution. The bitstream is considered random only if the p-value exceeds 0.01. For this test, the total result of the proportion over 19/20, is regarded as a pass.

the binary sequence (Fig. 5c). The pairwise HDs (Pair-HDs) for intra-and inter-devices among 20 tags are represented as a heatmap (Fig. 5d). Except for the diagonal areas in the contour, average values of the Pair-HDs are ~0.5. The false negative and positive rates are investigated theoretically (Fig. 5e). The false negative rate is the probability that an initially authenticated key fails to be authenticated. The false positive rate is the probability that one tag is falsely authenticated as another tag. If the distributions of the inter-tag and intra-tag variabilities do not overlap at all with each other, the false rates are zero. The cutoff threshold (HD = 0.189) returns to false positive- and negative- rates of the order of $10^{-12}$ for each case. Such low rates shore up the potential authentication applications with fine quality and security levels. A representative binary bitstream extracted from 20 different $MoS_x$ tags is shown in Fig. 5f. Each tag includes 128 bits. With a 2560-bit stream (128 × 20), NIST statistical test was conducted (Table 1)[35].

**Clonability of tags**. The clonability of tags is mainly associated with the expense of counterfeiting techniques. The motivation or intent to counterfeit products becomes unlikely when the cost of the product, including the expenses incurred in fabricating tags, is lower than the expenditure involved in employing counterfeiting techniques. However, again it depends on bulk preparations or a one-time approach by counterfeiting techniques. In the current work, a PDMS layer is coated on $MoS_x$ clusters to avoid duplication by molding techniques and therefore would be extremely difficult to duplicate. A similar approach has been implemented in other research works[36]. In addition, advanced characterization techniques can also be used to avoid cloning of tags but would be more expensive. Advanced characterization tools, currently in development, employ a sophisticated operation mechanism for extracting signal information, while offering a remarkably straightforward and user-friendly approach to reading tags[37].

**Conclusion**

The fabrication of random morphology of $MoS_x$ clusters inspired by capillary and Marangoni flows for anticounterfeiting tags is successfully demonstrated. The current approach not only enables the generation of random clusters but also facilitates the development of unique tags using advanced functional materials. Real-time observation of bulk cluster formation in droplet form provides compelling evidence for the realization of metal-oxide cluster formation during thin film processing. By utilizing confocal laser microscopy, the 3D physical dimensions of clusters were extracted and translated into quantitative information, which proved to be valuable for generating key outputs.

Additionally, the protective PDMS coating, which is transparent to visible wavelengths, prevents duplication through molding techniques while still allowing tag reading using confocal laser microscopy. The performance characteristics of the tags (keys), evaluated through mathematical tools, confirm their essential credibility and utility in anticounterfeiting technology.

## Methods

**Preparation of precursor solution and deposition of metal oxide films**. All chemicals were purchased from Sigma-Aldrich and used as received. A precursor solution was prepared by dissolving 0.05 M of ammonium heptamolybdate (($NH_4$)$_6$$Mo_7$$O_{24}$) in 5 ml of deionized water. The resulting solution was stirred on a magnetic stirrer at 3000 rpm for approximately 10 min for the complete dissolution of the inorganic compound. It was then filtered using a 25 µm micro-filter to remove any undissolved precipitates. Prior to spin-coating, the Si/$SiO_2$ substrate (3 × 3 cm$^2$) was sequentially cleaned using solvents (DI-acetone-DI) and treated with oxygen plasma (60 W and 60 sccm for 60 s). The precursor solution was then cast onto the Si/$SiO_2$ substrate at 3000 rpm for 60 s. Subsequently, the spin-coated substrate was placed on a preheated hot plate at 250 °C for 15 min, resulting in the formation of porous $MoO_x$ clusters, a few micrometers in size, randomly distributed throughout the substrate.

**Fabrication of $MoS_x$ PUF**. The film containing $MoO_x$ clusters was placed in a CVD chamber for sulfurization using $H_2S$ gas. A detailed explanation of this process can be found in the supporting information. The $MoS_x$ clusters were patterned into a 5 × 4 array, with each tag having an area of 50 × 50 µm$^2$, representing a total of 20 tags. Finally, a PDMS layer is coated on top of it to avoid duplication by molding techniques.

**Confocal laser microscopy**. A confocal laser microscopy (VK-X1050) was used to extract topography (3D patterns) in the XYZ planes from a physical device anticounterfeiting tag. The images were extracted by a laser diode with a wavelength of 661 nm, power of 6.0 µW, and 100× objective lens. The system has a maximum resolution in the XY, and Z planes are 10 nm and 5 nm.

**Programming**. All image processing and key extraction codes were implemented in Python (3.10.2) and Jupyter Notebook. After key extraction, tag characteristics related to statistics were analyzed using MATLAB.

## References
1. Deegan, R. D. et al. Capillary flow as the cause of ring stains from dried liquid drops. *Nature* **389**, 827–829 (1997).
2. Soltman, D. & Subramanian, V. Inkjet-printed line morphologies and temperature control of the coffee ring effect. *Langmuir* **24**, 2224–2231 (2008).
3. Pujar, P., Anusha, P., Gupta, D. & Mandal, S. Investigation of sintering kinetics and morphological evolution of silver films from nano-dispersion. *Appl. Phys. A* **124**, 831 (2018).
4. Kwak, B., Choi, S., Maeng, J. & Bae, J. Marangoni effect inspired robotic self-propulsion over a water surface using a flow-imbibition-powered microfluidic pump. *Sci. Rep.* **11**, 17469 (2021).

5.  Shin, J. W., Lim, H.-R., Cho, H.-B., Kwon, Y.-T. & Choa, Y.-H. Segregation-controlled self-assembly of silver nanowire networks using a template-free solution-based process. *Nanoscale* **13**, 8442–8451 (2021).
6.  Jung, D. et al. Highly conductive and elastic nanomembrane for skin electronics. *Science* **373**, 1022–1026 (2021).
7.  Kim, K. K. et al. Transparent wearable three-dimensional touch by self-generated multiscale structure. *Nat. Commun.* **10**, 2582 (2019).
8.  Blackstone, E. A., Fuhr, J. P. & Pociask, S. The health and economic effects of counterfeit drugs. *Am. Heal. Drug Benefits* **7**, 216–24 (2014).
9.  Clark, F. Rise in online pharmacies sees counterfeit drugs go global. *Lancet* **386**, 1327–1328 (2015).
10. Arppe, R. & Sørensen, T. J. Physical unclonable functions generated through chemical methods for anti-counterfeiting. *Nat. Rev. Chem.* **1**, 0031 (2017).
11. Bae, H. J. et al. Biomimetic microfingerprints for anti-counterfeiting strategies. *Adv. Mater.* **27**, 2083–2089 (2015).
12. Wali, A. et al. Biological physically unclonable function. *Commun. Phys.* **2**, 39 (2019).
13. Im, H. et al. Chaotic organic crystal phosphorescent patterns for physical unclonable functions. *Adv. Mater.* **33**, 2102542 (2021).
14. Liu, Y. et al. Inkjet-printed unclonable quantum dot fluorescent anti-counterfeiting labels with artificial intelligence authentication. *Nat. Commun.* **10**, 2409 (2019).
15. Song, B. et al. Fluorescent and magnetic anti-counterfeiting realized by biocompatible multifunctional silicon nanoshuttle-based security ink. *Nanoscale* **10**, 1617–1621 (2018).
16. Leem, J. W. et al. Edible unclonable functions. *Nat. Commun.* **11**, 328 (2020).
17. Kim, M. S. & Lee, G. J. Visually hidden, self-assembled porous polymers for optical physically unclonable functions. *ACS Appl. Mater. Interfaces* **15**, 4477–4486 (2023).
18. Deegan, R. D. et al. Contact line deposits in an evaporating drop. *Phys. Rev. E* **62**, 756–765 (2000).
19. Hu, H. & Larson, R. G. Marangoni effect reverses coffee-ring depositions. *J. Phys. Chem. B* **110**, 7090–7094 (2006).
20. Pujar, P., Gandla, S., Gupta, D., Kim, S. & Kim, M. Trends in low-temperature combustion derived thin films for solution-processed electronics. *Adv. Electron. Mater.* **6**, 2000464 (2020).
21. Sanchez-Rodriguez, D. et al. Thermal analysis for low temperature synthesis of oxide thin films from chemical solutions. *J. Phys. Chem. C* **117**, 20133–20138 (2013).
22. Kim, J. H. et al. Nanoscale physical unclonable function labels based on block copolymer self-assembly. *Nat. Electron.* **5**, 433–442 (2022).
23. Cao, Y. et al. Optical identification using imperfections in 2D materials. *2D Mater* **4**, 045021 (2017).
24. Shao, B. et al. Crypto primitive of MOCVD MoS2 transistors for highly secured physical unclonable functions. *Nano Res.* **14**, 1784–1788 (2021).
25. Alharbi, A., Armstrong, D., Alharbi, S. & Shahrjerdi, D. Physically unclonable cryptographic primitives by chemical vapor deposition of layered MoS$_2$. *ACS Nano* **11**, 12772–12779 (2017).
26. Park, J. et al. Disordered heteronanostructures of MoS$_2$ and TiO$_2$ for unclonable cryptographic primitives. *ACS Appl. Nano Mater.* **4**, 2076–2085 (2021).
27. Buades, A., Coll, B. & Morel, J. Image denoising by non-local averaging. in *Proceedings. (ICASSP '05). IEEE International Conference on Acoustics, Speech, and Signal Processing*, vol. 2, 25–28 (IEEE) 2005.
28. Maes, R., van der Leest, V., van der Sluis, E. & Willems, F. Secure key generation from biased PUFs: extended version. *J. Cryptogr. Eng.* **6**, 121–137 (2016).
29. Che, W., Kajuluri, V., Martin, M., Saqib, F. & Plusquellic, J. Analysis of entropy in a hardware-embedded delay PUF. *Cryptography* **1**, 8 (2017).
30. Gong, M., Liu, H., Min, R. & Liu, Z. Pitfall of the strongest cells in static random access memory physical unclonable functions. *Sensors* **18**, 1776 (2018).
31. Herder, C., Yu, M.-D., Koushanfar, F. & Devadas, S. Physical unclonable functions and applications: a tutorial. *Proc. IEEE* **102**, 1126–1141 (2014).
32. Gandla, S., Moon, C., Baek, S., Park, H. & Kim, S. Laser-induced carbonization for anticounterfeiting Tags. *Adv. Funct. Mater.* **33**, (2023).
33. Maiti, A., Gunreddy, V. & Schaumont, P. A systematic method to evaluate and compare the performance of physical unclonable functions. in *Embedded Systems Design with FPGAs* 245–267 (Springer New York, https://doi.org/10.1007/978-1-4614-1362-2_11 2013).
34. Pappu, R., Recht, B., Taylor, J. & Gershenfeld, N. Physical one-way functions. *Science* **297**, 2026–2030 (2002).
35. Andrew L. et al. *A Statistical Test Suite for Random and Pseudorandom Number Generators for Cryptographic Applications*. (2001).
36. Jing, L. et al. Multigenerational crumpling of 2D materials for anticounterfeiting patterns with deep learning authentication. *Matter* **3**, 2160–2180 (2020).
37. Gu, Y. et al. Gap-enhanced Raman tags for physically unclonable anticounterfeiting labels. *Nat. Commun.* **11**, 516 (2020).

## Acknowledgements

## Author contributions

S.K. designed and supervised this project. P.P. and S.G. guided the whole experiment. C.M. and B.S. performed all the experiments except for confocal microscope measurement. D.K. and S.L. conducted confocal microscope measurement. P.P. performed the analysis of MoS$_x$ cluster forming based on marangoni and capillary flows. C.M. and K.K. conceived and performed the key extraction and key analysis. All the authors analyzed the data. C.M., P.P., S.G., K.K., and S.K. wrote the manuscript. All authors have approved the final version of the manuscript.

## Competing interests

The authors declare no competing interests

## Additional information

**Supplementary information** The online version contains supplementary material available at https://doi.org/10.1038/s43246-023-00424-w.

**Correspondence** and requests for materials should be addressed to Kon-Woo Kwon or Sunkook Kim.

**Peer review information** Communications Materials thanks the anonymous reviewers for their contribution to the peer review of this work. Primary Handling Editor: John Plummer. A peer review file is available.

**Reprints and permission information** is available at http://www.nature.com/reprints

**Publisher's note** Springer Nature remains neutral with regard to jurisdictional claims in published maps and institutional affiliations.